

FIG. 1: (Color online)  $\Delta E - E$  plot for  $^{89}\text{Y} + p$  (a), with the deposited energy in the thick  $E$  detector versus the thin  $\Delta E$  detector for  $\theta = 132 \pm 1^\circ$ , and (b) the sum of the deposited energy in the thin and thick detector for the same angle. The labeled peaks are the ground state (0), the first excited 909-keV level (1), the second excited 1507-keV level (2), and the third excited 1744-keV level (3).

clearly showing a strong increase at low  $\gamma$ -ray energies, in accordance with previous experimental [12, 13] and theoretical [14] findings in this mass region. We also investigate the impact of our results on capture cross sections and astrophysical reaction rates. More specifically, we consider the cases  $^{88}\text{Sr}(p, \gamma)^{89}\text{Y}$  and  $^{88}\text{Y}(n, \gamma)^{89}\text{Y}$ , as these are relevant for the  $p$ -process in this mass region, and are also of interest for reaction networks in the context of stockpile stewardship [15].

The paper is organized as follows. In Sec. II, experimental details and an overview of the data analysis are given. Shell-model calculations and models for the  $\gamma$ -ray strength function are presented in Sec. III. In Sec. IV, calculated cross sections and reaction rates are shown and compared with existing data. Finally, a summary and outlook can be found in Sec. V.

## II. EXPERIMENTAL DETAILS AND EXTRACTION OF LEVEL DENSITY AND $\gamma$ -STRENGTH FUNCTION

### A. Experimental details and unfolding of $\gamma$ spectra

The experiment was performed at the Oslo Cyclotron Laboratory (OCL), utilizing a proton beam of 17 MeV. The beam was impinging on a natural  $^{89}\text{Y}$  target with thickness  $2.25 \text{ mg/cm}^2$ . The beam current was typically  $\approx 0.5 \text{ nA}$ , with about 5 days of beam time, including calibration runs on a natural Si target.

Charged ejectiles were measured with the Silicon Ring (SiRi) array [16], which is a  $\Delta E - E$  telescope system of 8 individual telescopes, each consisting of a  $130\text{-}\mu\text{m}$  8-fold segmented front detector ( $\Delta E$ ) with a  $1500\text{-}\mu\text{m}$  back detector ( $E$ ) detector; hence, there are 64 individual silicon telescopes in the system. To reduce the amount of  $\delta$  electrons from the target, a  $10.5\text{-}\mu\text{m}$  thick aluminium foil was placed in front of SiRi. The SiRi system was mounted in backward angles, covering the range  $\theta = 126 - 140^\circ$  with an angular resolution

of  $\Delta\theta = 2^\circ$ . Typical particle spectra from the experiment is shown in Fig. 1. It is seen that the charged-particle species are clearly separated from each other. In the following, we gate on the protons, i.e. we consider the  $^{89}\text{Y}(p, p'\gamma)^{89}\text{Y}$  reaction channel. The proton-energy resolution was  $\approx 130 - 160 \text{ keV}$  (FWHM), determined from the ground-state peak and discrete peaks in the proton  $\Delta E + E$  spectrum.

The  $\gamma$  rays were detected with the high-efficiency NaI(Tl) array CACTUS [17]. For this experiment, CACTUS comprised 26 cylindrical NaI detectors of diameter 12.7 cm and length 12.7 cm mounted on the spherical CACTUS frame at angles  $\Theta = 37.4^\circ, 63.4^\circ, 79.3^\circ, 100.7^\circ, 116.6^\circ$ , and  $142.6^\circ$  with respect to the beam direction. All NaI crystals are collimated with lead cones to reduce the Compton contribution and enhance the peak-to-total ratio. The total efficiency for  $E_\gamma = 1.33 \text{ MeV}$  was  $\approx 14.1\%$ . The trigger for the analog-to-digital converters of the CACTUS array was the signal from the thick  $E$  detector in SiRi; this was also the start signal for the time-to-digital converters of the NaI detectors.

By selecting the proton channel and requiring the coincident  $\gamma$ -rays with the protons within a time window of  $\approx 20 \text{ ns}$ , we obtain  $\gamma$  spectra for each excitation energy, which is found from the measured proton energy in SiRi corrected for the reaction kinematics. The excitation-energy versus NaI signals are shown in Fig. 2a. Some pileup events are observed for  $E_\gamma > E_x$ , however, they are rare and do not contribute significantly. We also see contaminant  $\gamma$  lines from  $^{12}\text{C}$  and  $^{16}\text{O}$ , e.g., at  $E_\gamma = 4.4, 6.1$  and  $7.1 \text{ MeV}$ . These lines are kept in the data set for unfolding, and later removed as explained in the following.

The  $\gamma$ -ray spectra for each excitation energy bin were corrected for the CACTUS response functions, i.e. removing the Compton, single-escape, double escape, and back-scattered annihilation events, and correcting for the full-energy efficiency. The contamination lines were also unfolded to obtain only the full-energy peaks in the final, unfolded  $\gamma$ -ray

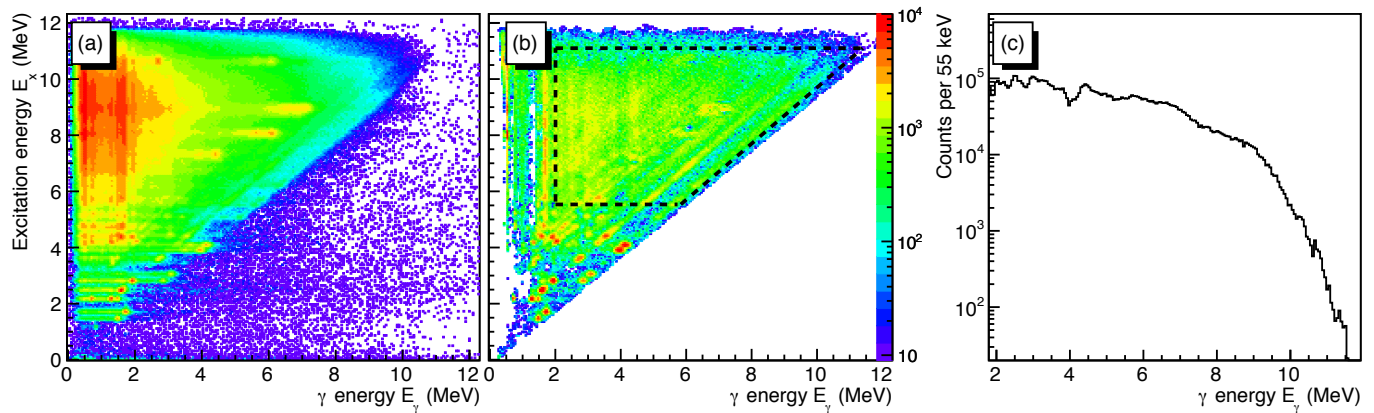


FIG. 2: (Color online) (a) Raw NaI spectra and (b) unfolded, primary  $\gamma$  spectra for each initial excitation-energy bin for  $^{89}\text{Y}(p, p'\gamma)^{89}\text{Y}$ ; the area within the dashed lines are used in the further analysis, i.e. the data for  $E_\gamma > 2.00$  MeV,  $5.43 < E_x < 10.98$  MeV are selected. (c) Projection of the primary  $\gamma$  spectra for the range of excitation energies between the lines.

spectra. Then, a 3D scan of the area around the full-energy peaks was performed to get a correct estimate of the underlying spectrum, and finally removing the carbon and oxygen lines. Experimental response functions have been recorded in-beam for  $\gamma$  transitions of  $^{13}\text{C}$ ,  $^{16}\text{O}$ ,  $^{28}\text{Si}$ , and  $^{56}\text{Fe}$ . The unfolding procedure is described in detail in Ref. [18]; the main advantage of this method is that the original, statistical fluctuations are preserved without introducing spurious fluctuations. This is obtained by applying a strong smoothing on the Compton background spectrum before subtracting it from the raw spectrum. This approach is justified by the fact that the Compton background varies slowly with  $\gamma$ -ray energy. Hence, we avoid spurious structures in the final, unfolded spectrum.

The experimental spin range for the present experiment can be inferred from both the singles-proton spectrum and the proton- $\gamma$  coincidences. From the unfolded proton- $\gamma$  coincidences, we clearly identify transitions for states with spin/parity up to  $7/2^+$ . From the singles-proton spectrum, we see that the 909-keV isomer with spin/parity  $9/2^+$  is populated. This provides a lower limit for the populated spins.

### B. Primary $\gamma$ -ray spectra and functional form of the level density and $\gamma$ -ray strength

Once the  $\gamma$ -spectra were properly unfolded, an iterative method [19] was applied to obtain the distribution of primary  $\gamma$  transitions from secondary and higher-order transitions. The principle of this method is that for a given excitation-energy bin  $j$ , this will contain all the  $\gamma$ -rays of the decay cascades from lower-lying bins  $i < j$ , and in addition the primary transitions for bin  $j$ . Thus, by subtracting a weighted sum of the spectra below  $j$ , the distribution of primary  $\gamma$  rays for bin  $j$  is obtained. Systematic uncertainties of this procedure is discussed in detail in Ref. [20]. The obtained matrix of primary  $\gamma$ -ray spectra is displayed in Fig. 2b, and the projection of the primary  $\gamma$  rays for  $E_x \approx 5.5 - 11.0$  MeV is shown in Fig. 2(b).

We note that the spectrum in Fig. 2(b) is rather smooth, although some structures appear particularly at lower  $E_\gamma$  values.

The data within the dashed lines are used for the extraction of NLD and  $\gamma$ SF in the next step. The boundaries are chosen for the following reasons: we need to make sure that the decay originates from a region of fairly high level density, and also that the primary  $\gamma$  spectra are indeed correct. An indicator for how well the primary- $\gamma$  extraction procedure works, is calculated for each iteration and for each excitation-energy bin. In short, this indicator shows whether the primary spectrum corresponds to a  $\gamma$  multiplicity of 1, which it obviously should, and in such cases the indicator is unity. We allow for a variation in this indicator of  $\pm 15\%$ ; if the deviation from unity is larger, we do not use the primary spectra from that excitation-energy region (see Ref. [19] for more details). Therefore, cuts are made in the matrices as shown in Fig. 2, ensuring relatively high initial excitation energies and thus high initial level density:  $E_x = 5.44 - 10.97$  MeV, and  $E_\gamma^{\text{low}} = 2.01$  MeV for  $^{89}\text{Y}$ . The  $E_\gamma^{\text{low}}$  limit is necessary because of strong, discrete transitions being either subtracted too little or too much below this energy, resulting in vertical "ridges" or "valleys" in the primary  $\gamma$  matrix (see also the discussion in Ref. [20]).

To extract the NLD and the  $\gamma$ SF from the set of primary  $\gamma$ -ray spectra, we make use of the following relation [10]:

$$P(E_\gamma, E_x) \propto \rho(E_f) \mathcal{T}(E_\gamma). \quad (1)$$

Here,  $P(E_\gamma, E_x)$  is the experimental primary  $\gamma$ -ray matrix as shown in Fig. 2, but where the primary  $\gamma$  spectra of each excitation-energy bin are normalized to unity to represent the probability of decay from that bin [10]. The matrix of primary  $\gamma$  spectra,  $P(E_\gamma, E_x)$ , is proportional to the level density at the final excitation energy  $E_f = E_x - E_\gamma$ , and to the  $\gamma$ -ray transmission coefficient  $\mathcal{T}(E_\gamma)$ . The latter is dependent on the  $\gamma$ -ray energy only, in accordance with the generalized form of the Brink-Axel hypothesis [21, 22]. The generalized Brink-Axel hypothesis has very recently been experimentally verified for  $\gamma$  transitions in the quasicontinuum [23]. The ex-

pression in Eq. (1) is valid for statistical decay, i.e. where the decay is independent of the formation of the compound state [24].

The functional form of the NLD and  $\gamma$ SF is determined through a least- $\chi^2$  fit to the  $P(E_\gamma, E_x)$  matrix as described in Ref. [10]. The absolute normalization of the functions remains to be found, i.e. determining the parameters  $\mathcal{A}$ ,  $\mathcal{B}$ , and  $\alpha$  in the transformations

$$\rho(E_x - E_\gamma) = \mathcal{A} \exp[\alpha(E_x - E_\gamma)] \tilde{\rho}(E_x - E_\gamma), \quad (2)$$

$$\mathcal{T}(E_\gamma) = \mathcal{B} \exp(\alpha E_\gamma) \tilde{\mathcal{T}}(E_\gamma), \quad (3)$$

which all give equally good fits to the experimental data. This normalization will be described in the following.

### C. Normalization of the level densities

To determine the absolute scaling  $\mathcal{A}$  and the slope  $\alpha$  of the level density, our data points are normalized to discrete levels [25] at low excitation energy. At the neutron separation energy  $S_n$ , data on average  $s$ -wave neutron-resonance spacings  $D_0$  [26], are usually used to calculate the total level density  $\rho(S_n)$  for all spins and both parities. For the case of  $^{89}\text{Y}$ , there are no neutron-resonance data available as  $^{88}\text{Y}$  is unstable. To estimate reasonable normalization parameters we have considered systematics of  $s$ -wave ( $\ell = 0$ ) resonance spacings for this mass region using the most recent evaluation of the Reference Input Parameter Library (RIPL-3, Ref. [26]). In addition, systematic errors due to the spin distribution at  $S_n$  must be taken into account [20]. This will be discussed in the following.

In our recent work [11], the  $^{89,90}\text{Y}$  level densities were normalized using global systematics of Ref. [27] within the constant-temperature (CT) approximation of the level-density function. This approach gives a very good description of the functional form of experimental level densities above  $\approx 2\Delta$  [28], where  $\Delta \approx 1$  MeV is the pair-gap parameter. However, it yields rather low (and constant) values for the spin-cutoff parameter. Moreover, this is only one out of several possible values for the spin-cutoff parameter and hence for the upper normalization point. Also, as the spin distribution for excitation energies up to the neutron separation energy is needed for the normalization of the  $\gamma$ SF later on, we will here rely on an excitation-energy dependent spin-cutoff parameter. We have chosen three different approaches, the first one using a phenomenological Fermi-gas (FG) spin cutoff parameter following Ref. [27] (FG09):

$$\sigma_{09}^2(E_x) = 0.391A^{0.675}(E_x - 0.5Pa')^{0.312}. \quad (4)$$

Here,  $E_x$  is the excitation energy,  $A$  is the mass number and  $Pa'$  is the deuteron pairing energy as defined in Ref. [27]. Secondly, we consider the FG spin cutoff parameter of Ref. [29], where a rigid-body moment of inertia is assumed (FG05):

$$\sigma_{05}^2(E_x) = 0.0146A^{5/3} \frac{1 + \sqrt{1 + 4a(E_x - E_1)}}{2a}. \quad (5)$$

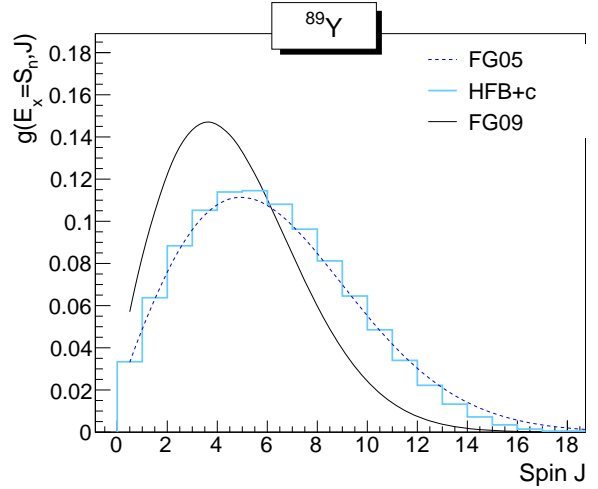


FIG. 3: (Color online) Spin distributions for  $^{89}\text{Y}$  at the neutron separation energy  $S_n = 11.482$  MeV for the three different normalization approaches. For FG09 and FG05, Eq. (6) is used with their respective spin cutoff parameters in Eqs. (4) and (5). The HFB+c calculations assume no specific shape of the spin distribution, but happens to be very similar to FG05 in this case.

Here,  $a$  is the level-density parameter and  $E_1$  is the excitation-energy backshift determined from global systematics of Ref. [29]. For the phenomenological spin cutoff parameters, the spin distribution is given by the standard expression [30, 31]:

$$g(E_x, J) \simeq \frac{2J+1}{2\sigma^2(E_x)} \exp\left[\frac{-(J+1/2)^2}{2\sigma^2(E_x)}\right]. \quad (6)$$

Using the phenomenological spin cutoff parameters and assuming equiparity (as shown in Ref. [11]), the total level density at  $S_n$  can be estimated from  $D_0$  through the expression [10]

$$\rho(S_n) = \frac{2\sigma^2}{D_0} \cdot \frac{1}{(J_t + 1) \exp[-(J_t + 1)^2/2\sigma^2] + J_t \exp[-J_t^2/2\sigma^2]}, \quad (7)$$

where  $J_t$  is the ground-state spin of the target nucleus in the neutron-resonance experiment. Finally, we use microscopic calculations within the Hartree-Fock-Bogoliubov plus combinatorial (HFB+c) approach [32]. The three spin distributions are shown in Fig. 3 for the case of  $^{89}\text{Y}$ .

We observe that the spin distribution of Eq. (6) using  $\sigma_{05}$  is very broad and centered at significantly higher spins than using  $\sigma_{09}$ . We consider therefore  $\sigma_{05}$  to give the upper limit, and  $\sigma_{09}$  as the lower limit in estimating  $\rho(S_n)$  for  $^{89,90}\text{Y}$ . The calculated  $\rho(S_n)$  values for Rb, Sr, Y, and Zr isotopes are given in Table I together with the applied input parameters. The resulting systematics for the level densities at  $S_n$  are shown in Fig. 4. Note that the predictions from the global systematics are fitted to the semi-experimental data points through a common scaling factor of  $0.31^{+0.09}_{-0.10}$  and  $0.34^{+0.08}_{-0.07}$  for  $\rho_{05,09}(S_n)$ , respectively. Using the upper (lower)  $\chi^2$  uncertainty for the

TABLE I: Neutron resonance parameters  $D_0$  and  $\langle \Gamma_{\gamma 0} \rangle$  from Ref. [26], and spin cutoff parameters from global systematics of Refs. [27, 29];  $A_f$  is the final nucleus following neutron capture,  $J_i$  is the ground-state spin of the target nucleus,  $S_n$  is the neutron-separation energy,  $\sigma_{05,09}$  are the spin-cutoff parameters from Eqs. (4) and (5),  $D_0$  is the  $s$ -wave level spacing [26], and  $\rho_{05,09}(S_n)$ , are the total level densities calculated from  $\sigma_{05,09}$ . Finally,  $\rho_{05,09}^{\text{syst}}$  are the total level densities at  $S_n$  as predicted from the global systematics of Refs. [27, 29], respectively.

$A_f$	$J_i$	$S_n$ (MeV)	$D_0$ (keV)	$\sigma_{05}(S_n)$	$\rho_{05}(S_n)$ ( $10^4 \text{ MeV}^{-1}$ )	$\rho_{05}^{\text{syst}}(S_n)$ ( $10^4 \text{ MeV}^{-1}$ )	$\sigma_{09}(S_n)$	$\rho_{09}(S_n)$ ( $10^4 \text{ MeV}^{-1}$ )	$\rho_{09}^{\text{syst}}(S_n)$ ( $10^4 \text{ MeV}^{-1}$ )	$\langle \Gamma_{\gamma 0} \rangle$ (meV)
$^{86}\text{Rb}$	5/2	8.651	0.172(8)	5.12	6.11(28)	21.6	4.02	4.22(20)	12.4	250(10)
$^{88}\text{Rb}$	3/2	6.083	1.630(150)	4.80	0.78(7)	1.47	3.85	0.53(5)	1.14	170(30)
$^{85}\text{Sr}$	0	8.530	0.320(120)	4.89	15.3(57)	20.4	3.91	9.88(370)	7.88	240(80)
$^{87}\text{Sr}$	0	8.424	2.600(800)	5.07	2.02(62)	13.2	3.94	1.23(38)	4.01	260(80)
$^{88}\text{Sr}$	9/2	11.11	0.290(80)	5.22	3.00(83)	13.1	4.02	2.44(67)	6.40	150(40)
$^{89}\text{Sr}$	0	6.359	23.70(290)	4.72	0.19(2)	0.53	3.76	0.12(2)	0.39	190(50)
$^{90}\text{Y}$	1/2	6.857	3.700(400)	4.99	0.70(8)	2.25	3.93	0.44(5)	1.71	130(40)
$^{91}\text{Zr}$	0	7.194	6.000(1400)	4.95	0.83(19)	1.20	3.88	0.52(12)	0.91	130(20)
$^{92}\text{Zr}$	5/2	8.635	0.550(100)	5.03	1.85(34)	4.11	3.95	1.29(23)	2.60	140(40)
$^{93}\text{Zr}$	0	6.734	3.500(800)	4.84	1.37(31)	1.69	3.86	0.88(20)	1.31	135(25)
$^{94}\text{Zr}$	5/2	8.221	0.302(75)	4.95	3.29(82)	5.62	3.94	2.34(58)	3.63	157(20)
$^{95}\text{Zr}$	0	6.462	4.000(800)	4.79	1.17(24)	1.99	3.86	0.77(15)	1.54	85(20)
$^{97}\text{Zr}$	0	5.575	13.00(300)	4.66	0.34(8)	0.58	3.76	0.23(5)	0.72	65(15)

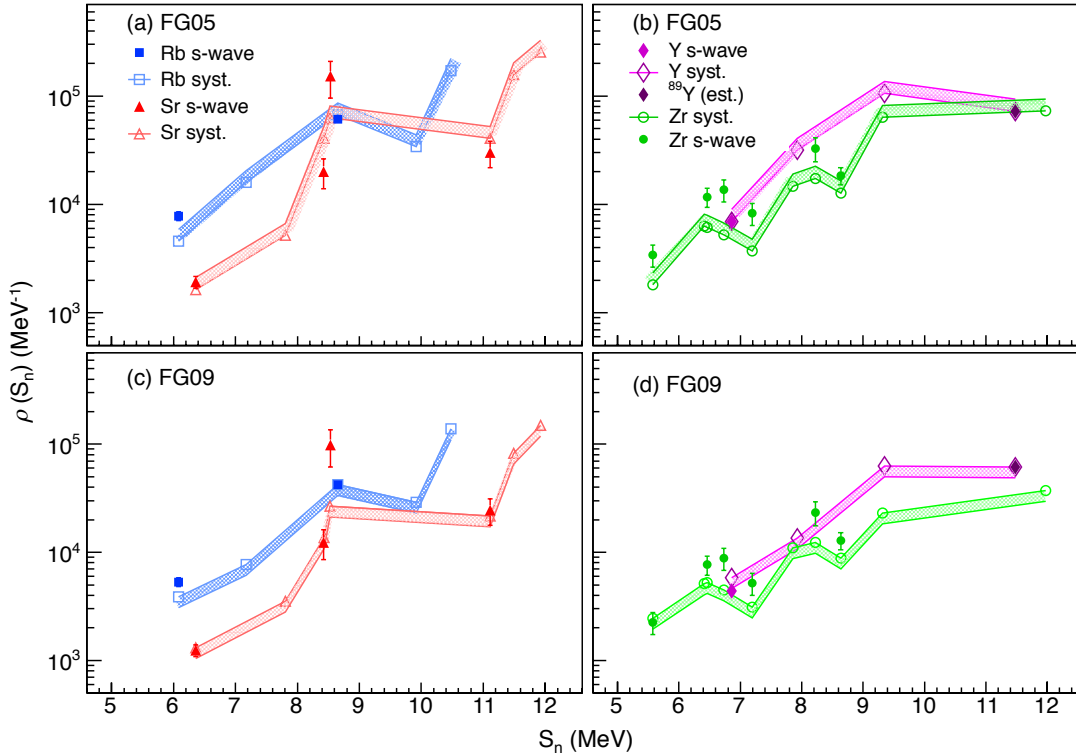


FIG. 4: (Color online) Level densities at  $S_n$  in the Y mass region with global systematics of (a-b) Ref. [29] (FG05) and (c-d) Ref. [27] (FG09) (see Table I). The unknown level density for  $^{89}\text{Y}$  is shown as a purple diamond. The global-systematics predictions are scaled with a factor of 0.31 and 0.34 for the FG05 and FG09 approaches, respectively. The error bands show the upper-limit scaling of 0.40 for FG05 (a-b) and the lower limit of 0.27 for FG09 (c-d).

$\sigma_{05}$  ( $\sigma_{09}$ ) results, we get the following estimates for  $^{89}\text{Y}$  ( $S_n = 11.482 \text{ MeV}$ ):  $\rho_{09}^{\text{low}}(S_n) = 4.87 \cdot 10^4 \text{ MeV}^{-1}$ , corresponding

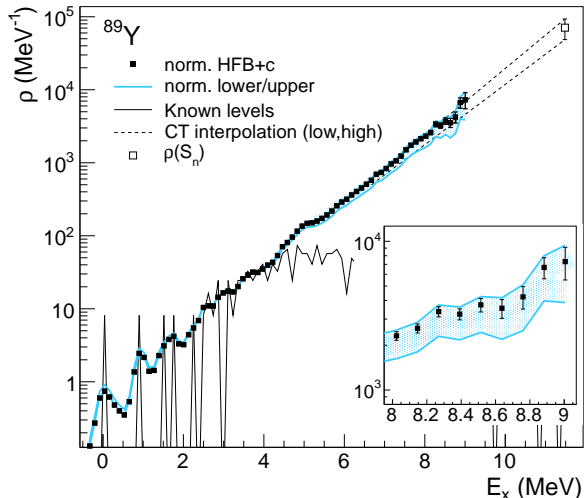


FIG. 5: (Color online) The extracted level density of  $^{89}\text{Y}$ . The black points give the HFB+c normalization, the lower and upper limits are shown as azure lines. The insert shows a zoom of the high- $E_x$  part.

to  $D_0 = 143$  eV for  $\sigma_{09}(S_n) = 4.12$ , and  $\rho_{05}^{\text{up}}(S_n) = 9.33 \cdot 10^4$   $\text{MeV}^{-1}$ , corresponding to  $D_0 = 100$  eV for  $\sigma_{05}(S_n) = 5.45$ . Finally, the HFB+c calculations (with no excitation-energy shift,  $\delta = 0.0$  MeV where  $\delta$  is defined in Ref. [32]) yield  $\rho_{\text{HFB+c}}(S_n) = 7.09 \cdot 10^4$   $\text{MeV}^{-1}$  with  $D_0 = 121$  eV. A fit of Eq. (6) on the HFB+c calculations at  $S_n$  gives  $\sigma_{\text{HFB+c}} = 4.89$ , i.e. in between the two phenomenological approaches.

Due to the cutoff on the  $\gamma$  energy,  $E_\gamma^{\text{low}}$  (see Fig. 2), our level-density data points will reach a maximum excitation energy of  $S_n - E_\gamma^{\text{low}}$ . Following Ref. [11], we use an interpolation between our data points up to  $\rho(S_n)$  of the constant-temperature form [30]:

$$\rho_{\text{CT}}(E_x) = \frac{1}{T} \exp \frac{E_x - E_0}{T}, \quad (8)$$

where  $E_0$  is the excitation-energy shift and  $T$  is the constant nuclear temperature. For  $^{89}\text{Y}$ , we have used  $(E_0, T) = (0.658, 0.95)$ ,  $(0.069, 1.02)$ , and  $(0.098, 1.05)$  MeV for FG05, HFB+c, and FG09 respectively.

The normalized level density is shown in Fig. 5. Our data points follow the discrete levels well up to  $E_x \approx 4.5$  MeV, which means that these levels are populated by primary  $\gamma$  decay from the higher-lying levels in the region; above this energy the level densities increase rapidly, while the known levels show a saturation when reaching  $\approx 65$   $\text{MeV}^{-1}$ . As discussed in Ref. [11], the level density displays a remarkable constant-temperature behavior. The lower and upper limits for the normalization are also shown, representing the systematic errors. Note that the lower limit is very similar to the normalization used in Ref. [11] (within 18%). At low excitation energies there is obviously not much difference between the normalization options, as our data points are fixed to the discrete levels. At the neutron separation energy the system-

atic uncertainty is at its maximum, within a factor of  $\approx 2$  (see insert of Fig. 5).

#### D. $\gamma$ -ray strength function

The slope of the  $\gamma$ SFs is determined through the normalization of the level densities (see Eqs. (2) and (3)). The absolute scale  $\mathcal{B}$  can be found by use of the total, average radiative width  $\langle \Gamma_{\gamma 0} \rangle$ . The average radiative width of neutron s-wave capture resonances with spins  $J_t \pm 1/2$  expressed in terms of the experimental  $\mathcal{T}$  is given by [33]:

$$\begin{aligned} \langle \Gamma_{\gamma 0}(S_n, J_t \pm 1/2, \pi_t) \rangle &= \frac{\mathcal{B}}{4\pi\rho(S_n, J_t \pm 1/2, \pi_t)} \int_{E_\gamma=0}^{S_n} dE_\gamma \mathcal{T}(E_\gamma) \\ &\times \rho(S_n - E_\gamma) \sum_{J=-1}^1 g(S_n - E_\gamma, J_t \pm 1/2 + J), \end{aligned} \quad (9)$$

where  $J_t$  and  $\pi_t$  are the spin and parity of the target nucleus in the  $(n, \gamma)$  reaction,  $\rho(S_n - E_\gamma)$  is the normalized, experimental level density obtained in Sec. II C, and  $\mathcal{T}$  is the experimental transmission coefficient, which in principle includes all types of electromagnetic transitions:  $\mathcal{T}_{E1} + \mathcal{T}_{M1} + \mathcal{T}_{E2} + \dots$ . The sum runs over all final states with spins  $J_t \pm 1/2 + J$ , where  $J = -1, 0, 1$  from considering the spins reached after one primary dipole transition with energy  $E_\gamma$  (see also Eq. (3.1.) in Ref. [34]). Note that the factor  $1/\rho(S_n, J_t \pm 1/2, \pi_t)$  equals the neutron resonance spacing  $D_0$ . From the normalized transmission coefficient, the  $\gamma$ SF is determined by

$$f(E_\gamma) = \frac{\mathcal{T}(E_\gamma)}{2\pi E_\gamma^3}, \quad (10)$$

using the fact that dipole transitions dominate the strength for the considered  $E_x$  region [34, 35].

For  $^{89}\text{Y}$ , we have estimated the unknown  $\langle \Gamma_{\gamma 0} \rangle$  from data in this mass region [26]. Specifically, we took the average value of the nuclei close in mass to  $^{89}\text{Y}$ , namely  $^{88,89}\text{Sr}$ ,  $^{90}\text{Y}$ , and  $^{91}\text{Zr}$ , see Table I. With an uncertainty of  $\approx 25\%$ , we obtain  $\langle \Gamma_{\gamma 0} \rangle(^{89}\text{Y}) = 150(38)$  meV. The assumed uncertainty of 25% is strongly guided by the comparison with photo-nuclear data from the reactions  $^{89}\text{Y}(\gamma, n) + ^{89}\text{Y}(\gamma, np)$  [36–38]. These cross-section data are converted into  $\gamma$ SF by the relation [26]

$$f(E_\gamma) = \frac{\sigma_{(\gamma, n)}(E_\gamma)}{3\pi^2 \hbar^2 c^2 E_\gamma}, \quad (11)$$

again assuming that dipole radiation is dominant, which is reasonable in this  $E_\gamma$  region (see e.g. [26] and references therein).

The normalized  $\gamma$ SF is shown in Fig. 6. The error bands include the uncertainty in  $\langle \Gamma_{\gamma 0} \rangle$  as well as in the level density and the choice of spin distribution. The uncertainty in absolute value ranges from a factor of 1.8 at  $E_\gamma = 2.0$  MeV to  $\approx 4.8$  at  $E_\gamma = 11.3$  MeV.

For  $\gamma$ -ray energies above 3–4 MeV, we find that the strength is increasing as a function of  $\gamma$ -ray energy, as expected for the tail of the giant dipole resonance (GDR) [39].

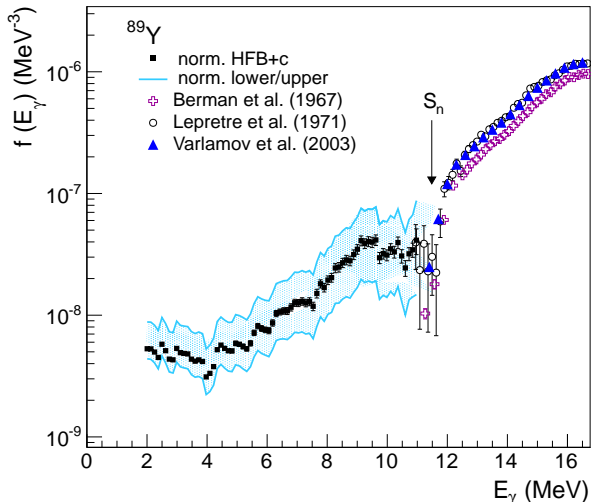


FIG. 6: (Color online) Normalized  $\gamma$ SF of  $^{89}\text{Y}$  compared to  $^{89}\text{Y}(\gamma, n) + ^{89}\text{Y}(\gamma, np)$  data from Refs. [36, 37], and evaluated data from Ref. [38]. The black points are obtained with the HFB+c normalization, the azure lines show the lower and upper limits.

We also observe a drop in strength for  $\gamma$  rays between  $\approx 9.6 - 11.0$  MeV. This is understood by looking at the primary  $\gamma$ -ray matrix in Fig. 2a, where it is clear that the upper right corner in the triangle has significantly fewer statistics than for lower  $\gamma$ -ray energies. This could be due to less direct feeding to the ground state, with spin/parity  $1/2^-$ , and more to the first excited  $9/2^+$  state at 909 keV. We note that this behavior is in agreement with the  $(\gamma, \gamma')$  data from Ref. [40], which also display a reduction in intensity in the energy range  $E_\gamma \approx 9.8 - 11.3$  MeV. This indicates that in this particular region, the extracted data are not representative for a general  $\gamma$ SF, because there is, very likely, a strong dependence on the final state(s) and the individual overlap with the initial and final state(s) of the transition(s).

Our data show an increase at decreasing  $\gamma$  energies for  $E_\gamma < 4$  MeV. This phenomenon, hereafter called the *upbend*, has been subject of great interest recently, and was first discovered in iron isotopes about a decade ago [41]. In Ref. [20], simulations on  $^{57}\text{Fe}$  using the DICEBOX code [42] suggested that an enhancement in the  $E1$  strength could be invoked, although it was not present in the input  $E1$  strength for the simulation. It was stressed that the low-energy enhancement could not be due to artifacts in the unfolding or the method for extracting primary transitions, as the same feature was seen using the primary transitions directly from the DICEBOX simulations. Three main reasons for this behavior was pointed out:

- (i) There was no significant contribution from quadrupole (E2) transitions in the simulations;
- (ii) Specific restrictions were applied on the initial spin population;

- (iii) The level density was very low for high spins in this particular simulation.

Hence, the simulations indicated an increase in the low-energy part of the  $\gamma$ SF in cases where the level density is low and the reaction populates selectively high spins and a rather narrow spin range.

However, this hypothesis was disproved in Ref. [13], where a different and virtually model-independent technique was applied on data from the  $^{94}\text{Mo}(d, p\gamma\gamma)^{95}\text{Mo}$  reaction. In contrast to the  $^{96}\text{Mo}(^3\text{He}, \alpha)^{95}\text{Mo}$  data from Ref. [12], where the reaction favors high- $\ell$  transfer, the (d, p) reaction mainly populates low- $\ell$  states. Nevertheless, the same shape of the  $\gamma$ SF was found [13]. Furthermore, using the Oslo method, it was shown in Ref. [35] that the  $^{56}\text{Fe}(p, p')^{56}\text{Fe}$  and the  $^{57}\text{Fe}(^3\text{He}, \alpha)^{56}\text{Fe}$  data sets yielded very similar  $\gamma$ SFs. Therefore, considering the available data as of today, other explanations must be sought for to explain the upbend feature.

The upbend has recently been shown to be dominantly of dipole nature in  $^{56}\text{Fe}$  [35] and in  $^{151,153}\text{Sm}$  [43], but the electromagnetic character is not known at present. Theoretical attempts suggest that both  $E1$  as well as  $M1$  strength may contribute. An enhancement of  $E1$  type is predicted from a thermal coupling of quasiparticles to the continuum of unbound states at relatively high temperature [44], whereas an enhancement of  $M1$  strength is found in shell-model calculations [14, 45]. Moreover, the presence of the upbend may enhance astrophysical  $(n, \gamma)$  rates of exotic neutron-rich nuclei by up to 2 orders of magnitude [46]. In the following, we will present shell-model calculations as well as models for the  $E1$  strength, and compare with our data.

### III. SHELL-MODEL CALCULATIONS AND MODELS FOR THE DIPOLE STRENGTH

The shell-model calculations were performed by means of the code RITSSCHIL [47] using a model space composed of the  $(0f_{5/2}, 1p_{3/2}, 1p_{1/2}, 0g_{9/2})$  proton orbits and the  $(0g_{9/2}, 1d_{5/2}, 0g_{7/2})$  neutron orbits relative to a  $^{68}\text{Ni}$  core. This configuration space was also applied in our earlier study of  $M1$  strength functions in  $^{94,95,96}\text{Mo}$  and  $^{90}\text{Zr}$  [14]. In the present calculations, two protons were allowed to be lifted from the  $fp$  shell to the  $0g_{9/2}$  orbit and two neutrons from the  $0g_{9/2}$  to the  $1d_{5/2}$  orbit. This resulted in dimensions up to 29000. The additional inclusion of the  $\nu(0g_{7/2})$  orbit has negligible influence on the low-energy part of the strength function, but produces a few strong  $M1$  transitions around 7 MeV dominated by the  $\nu(0g_{9/2})^{-1}\nu(0g_{7/2})$  spin-flip configuration (cf. Ref. [14]). As these transitions do not describe the spin-flip peak completely up to high energy, we use a phenomenological description for the spin-flip resonance in the present work.

The calculations included states with spins from  $J = 1/2$  to  $21/2$  for  $^{89}\text{Y}$ . For each spin the lowest 40 states were calculated. Reduced transition probabilities  $B(M1)$  were calculated for all transitions from initial to final states with energies  $E_f < E_i$  and spins  $J_f = J_i, J_i \pm 1$ . For the minimum

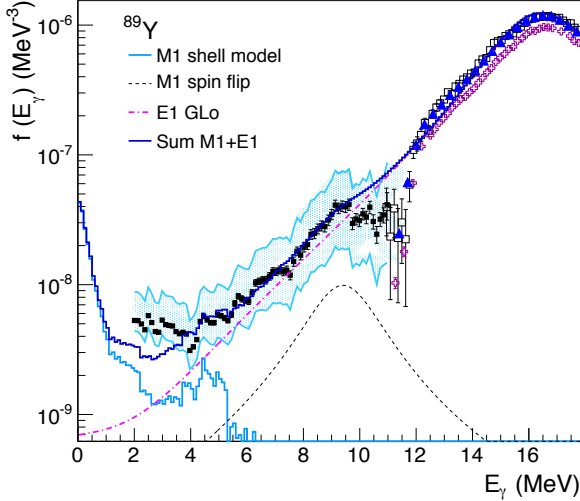


FIG. 7: (Color online) The  $\gamma$ SF of  $^{89}\text{Y}$  together with photo-nuclear data [36, 37] and evaluated  $(\gamma, n)$  data from Ref. [38], compared to models for the dipole strength.

and maximum  $J_i$ , the cases  $J_f = J_i - 1$  and  $J_f = J_i + 1$ , respectively, were excluded. This resulted in more than 32000  $M1$  transitions for each parity  $\pi = +$  and  $\pi = -$ , which were sorted into 100 keV bins according to their transition energy  $E_\gamma = E_i - E_f$ . The average  $B(M1)$  value for one energy bin was obtained as the sum of all  $B(M1)$  values divided by the number of transitions within this bin.

The  $M1$  strength functions were deduced using the relation

$$f_{M1}(E_\gamma) = \frac{16\pi}{9(\hbar c)^3} \overline{B}(M1, E_\gamma) \rho(E_i). \quad (12)$$

They were calculated by multiplying the  $B(M1)$  value in  $\mu_N^2$  of each transition with  $11.5473 \times 10^{-9}$  times the level density at the energy of the initial state  $\rho(E_i)$  in  $\text{MeV}^{-1}$  and deducing averages in energy bins as done for the  $\overline{B}(M1)$  values (see above). The level densities  $\rho(E_i, \pi)$  were determined by counting the calculated levels within energy intervals of 1 MeV for the two parities separately. The strength functions obtained for the two parities were subsequently added. When calculating the strength functions, gates were set on the excitation energy  $E_x$  that correspond to the ones applied in the analysis of the experimental data (see Sec. II). The resulting  $M1$  strength function for  $^{89}\text{Y}$  is shown in Fig. 7. The low-energy behavior of this strength function is very similar to that of the strength functions calculated for the neighboring nuclei  $^{94,95,96}\text{Mo}$ ,  $^{90}\text{Zr}$  [14] and for  $^{56,57}\text{Fe}$  [45].

The low-energy enhancement of  $M1$  strength is caused by transitions between many close-lying states of all considered spins located above the yrast line in the transitional region to the quasi-continuum of nuclear states. Inspecting the wave functions, one finds large  $B(M1)$  values for transitions between states that contain a large component (up to about 50%) of the same configuration with broken pairs of both

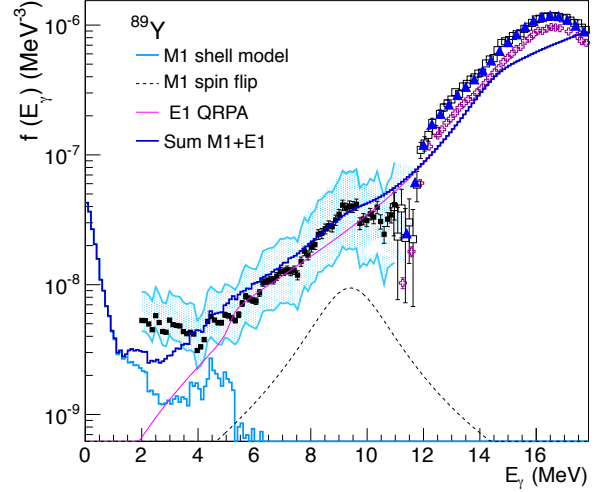


FIG. 8: (Color online) Same as Fig. 7 but with the QRPA  $E1$  strength (see text).

protons and neutrons in high- $j$  orbits, whereas states containing the unpaired  $1p_{1/2}$  proton and proton excitations only are not depopulated by strong  $M1$  transitions. The largest  $M1$  matrix elements connect configurations with the spins of high- $j$  protons re-coupled with respect to those of high- $j$  neutrons to the total spin  $J_f = J_i, J_i \pm 1$ . The corresponding main configurations for negative-parity states in  $^{89}\text{Y}$  are generated by exciting neutrons over the shell gap at  $N = 50$ , such as  $\pi(1p_{1/2}^{-1} \nu(0g_{9/2}^{-1} 1d_{5/2}^1))$  or  $\pi(1p_{1/2}^{-1} \nu(0g_{9/2}^{-2} 1d_{5/2}^2))$  and by additional proton excitations within the  $(fp)$  shell, i.e.  $\pi[(0f_{5/2}, 1p_{3/2})^{-1} 1p_{1/2}^2] \nu(0g_{9/2}^{-1} 1d_{5/2}^1)$  and also proton excitations over the subshell gap at  $Z = 40$ ,  $\pi[(0f_{5/2}, 1p_{3/2})^{-1} 1p_{1/2}^0 0g_{9/2}^2] \nu(0g_{9/2}^{-1} 1d_{5/2}^1)$ . The positive-parity states require the excitation of an  $(fp)$  proton to the  $0g_{9/2}$  orbit, for example  $\pi(1p_{3/2}^{-1} 1p_{1/2}^1 0g_{9/2}^1) \nu(0g_{9/2}^{-1} 1d_{5/2}^1)$ . The orbits in these configurations have large  $g$  factors with opposite signs for protons and neutrons. Combined with specific relative phases of the proton and neutron partitions they cause large total magnetic moments.

For a comparison with the experimental data, an  $E1$  contribution to the strength function has to be added. We have chosen two ways to estimate the  $E1$  strength: (i) the phenomenological Generalized Lorentzian (GLO) model [34], and (ii) a microscopic approach based on the quasiparticle-random-phase approximation (QRPA) [48, 49]. For option (i), we apply the GLO model with a constant temperature of the final states  $T_f$ , in contrast to a variable temperature which depends on the final excitation energy. The choice of a constant temperature is in accordance with the Brink hypothesis [21] and our ansatz that the  $\gamma$ -transmission coefficient is, on average, independent of excitation energy in the statistical  $E_x$  region. This is also in accordance with the constant-temperature level



TABLE II: Parameters used for the model strength functions of  $^{89}\text{Y}$  in Figs. 7, 8.

Nucleus	$\Gamma_{E1}$ (MeV)	$E_{E1}$ (MeV)	$\sigma_{E1}$ (mb)	$T_f$ (MeV)	$\Gamma_{M1}$ (MeV)	$E_{M1}$ (MeV)	$\sigma_{M1}$ (mb)	$\delta_{\text{QRPA}}$ (MeV)
$^{89}\text{Y}$	4.3	16.8	233.0	0.30	2.7	9.5	1.1	1.5

density found for  $^{89}\text{Y}$ . The GLo model is then given by

$$f_{\text{GLo}}(E_\gamma, T_f) = \frac{1}{3\pi^2\hbar^2 c^2} \sigma_{E1} \Gamma_{E1} \times \left[ \frac{E_\gamma \Gamma(E_\gamma, T_f)}{(E_\gamma^2 - E_{E1}^2)^2 + E_\gamma^2 \Gamma(E_\gamma, T_f)^2} + 0.7 \frac{\Gamma(E_\gamma = 0, T_f)}{E_{E1}^3} \right], \quad (13)$$

with

$$\Gamma(E_\gamma, T_f) = \frac{\Gamma_{E1}}{E_{E1}^2} (E_\gamma^2 + 4\pi^2 T_f^2). \quad (14)$$

The parameters  $\Gamma_{E1}$ ,  $E_{E1}$  and  $\sigma_{E1}$  correspond to the width, centroid energy, and peak cross section of the GDR. For option (ii), the  $E1$  strength is obtained from large-scale QRPA calculations on top of a Skyrme-Hartree-Fock-Bogoliubov description of the ground state. The QRPA calculations are performed in the spherical approximation, and a folding procedure is applied to obtain the correct spreading width of the GDR. For more details on the QRPA calculations, we refer the reader to Ref. [49]. The  $E1$  calculations were taken from the BRUSLIB library [50].

We included an  $M1$  spin-flip resonance with a standard-Lorentzian form [26], using parameters in accordance with a recent  $(p, p')$  $^{90}\text{Zr}$  experiment [51]. Strong  $M1$  transitions were also observed in a photon-scattering experiment in the excitation-energy region  $\approx 8 - 10$  MeV [52]. For the QRPA calculation, we had to shift the  $E1$  strength with an energy shift of  $\delta_{\text{QRPA}} = +1.5$  MeV, i.e.  $E_\gamma^{\text{new}} = E_\gamma + \delta_{\text{QRPA}}$ , so as to match the GDR data reasonably well around  $E_\gamma = 12$  MeV. The resulting theoretical dipole strengths are displayed in Figs. 7 and 8 for the best reproduction of the HFB+c normalization. All the parameters used for the shown models are listed in Table II.

In the following, we will use our experimentally inferred lower and upper limits on the level density and  $\gamma\text{SF}$  as input for cross-section calculations of the  $^{88}\text{Y}(n, \gamma)^{89}\text{Y}$  and  $^{88}\text{Sr}(p, \gamma)^{89}\text{Y}$  reactions.

#### IV. CROSS SECTION AND RATE CALCULATIONS

As discussed in the introduction, level density and  $\gamma\text{SF}$  are two key ingredients in the Hauser-Feshbach approach to calculate cross sections. In this work, we use the open-source nuclear reaction code TALYS-1.6 [53, 54] for the cross-section and reaction-rate calculations for the  $^{88}\text{Sr}(p, \gamma)^{89}\text{Y}$  and  $^{88}\text{Y}(n, \gamma)^{89}\text{Y}$  reactions. Our approach is the following:

1. Making use of all the various models already implemented in TALYS for the level density, the  $\gamma\text{SF}$ , and the proton and neutron optical potentials to investigate the spread in the resulting cross sections and reaction rates; i.e., inferring the lower and upper limits on these quantities inherent from the available models;
2. Calculating the cross sections and reaction rates with default input parameters in TALYS;
3. Implementing level densities and  $\gamma\text{SF}$ s in accordance with our present data and the experimentally inferred lower/upper limits.

##### 1. TALYS predictions for the model uncertainties.

We have calculated all possible combinations of input level densities,  $\gamma\text{SF}$  models, and optical potentials available in TALYS to estimate the minimum and maximum  $^{88}\text{Y}(n, \gamma)^{89}\text{Y}$  and  $^{88}\text{Sr}(p, \gamma)^{89}\text{Y}$  cross sections predicted by these models. For the  $(n, \gamma)$  reaction, the combinations are: (i) a minimum cross section and rate with the temperature-dependent Hartree-Fock-Bogoliubov plus combinatorial level density of Ref. [57], the  $E1$  strength function from the Hartree-Fock-BCS plus QRPA approach of Ref. [58] making use of the renormalization to the estimated  $\langle \Gamma_\gamma \rangle = 170$  meV from a spline-fit interpolation table in TALYS, and the JLM neutron potential [56] (TALYS keywords *ldmodel 6, strength 3, gnorm -1., jlmomp y*); (ii) a maximum cross section and rate with the combined constant-temperature plus back-shifted Fermi gas model [59] for the level density with parameters according to the TALYS manual, the standard Lorentzian model (Brink-Axel) for the  $E1$  strength [21, 22], and a global parameterization of the neutron optical potential [55] (TALYS keywords *ldmodel1, strength2, localomp n*). The corresponding combinations for the  $(p, \gamma)$  reaction are: (i) a minimum cross section and rate with the temperature-dependent Hartree-Fock-Bogoliubov plus combinatorial level density of Ref. [57], the GLo model [34] with variable temperature as implemented in TALYS renormalized to the spline-fit  $\langle \Gamma_\gamma \rangle$ , and the global parameterization of the proton optical potential [55] (TALYS keywords *ldmodel 6, strength 1, gnorm -1., localomp n*); (ii) a maximum cross section and rate with the combined constant-temperature plus back-shifted Fermi gas model [59] for the level density with parameters according to the TALYS manual, the standard Lorentzian model (Brink-Axel) for the  $E1$  strength [21, 22], and the JLM proton potential [56] (TALYS keywords *ldmodel 1, strength 2, jlmomp y*).

We find that the level density models in TALYS give a factor of  $\approx 5$  and  $\approx 4$  uncertainty for the  $(n, \gamma)$  and  $(p, \gamma)$  cross sections, respectively, while the corresponding numbers for the  $\gamma\text{SF}$  models are  $\approx 30$  and  $\approx 28$ , respectively. The impact of the choice of optical-model potential has also been tested for the reactions of interest. More specifically, we have used the proton and neutron potentials of Koning and Delaroche [55] with global parameters as described in the TALYS manual, and also the semi-microscopic optical potential of the Jeukenne-Lejeune-Mahaux (JLM) type [56]; see the TALYS documentation for more details [53, 54]. We did not adjust any parameters in the neutron or proton potentials, but

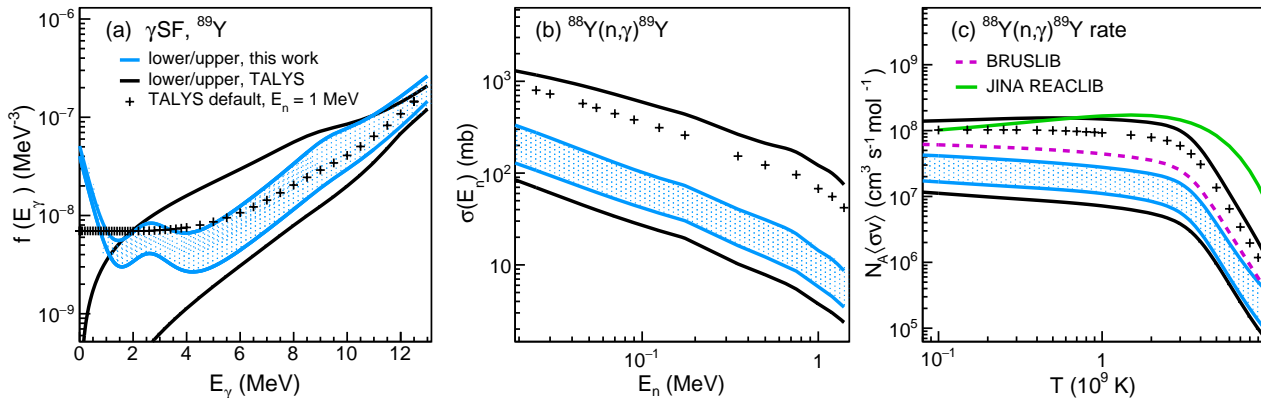


FIG. 9: (Color online) (a) Input  $\gamma$ SFs of  $^{89}\text{Y}$ , note that the TALYS default is for  $E_n = 1$  MeV, corresponding to an initial excitation energy of 12.48 MeV in the GLo Model, and that the GLo model is by default normalized to a radiative width  $\langle\Gamma_\gamma\rangle = 170$  meV taken from an interpolation routine in TALYS; (b) the resulting  $^{88}\text{Y}(n,\gamma)^{89}\text{Y}$  cross sections, (c) and the corresponding astrophysical reaction rates compared to the BRUSLIB (dashed magenta line, Ref. [50]) and the JINA REACLIB (green solid line, Ref. [62]). The minimum and maximum predictions from the models implemented in TALYS are also shown (thick, black lines).

TABLE III: Parameters used for the  $\gamma$ SF input models in the TALYS calculations.

	$\Gamma_{E1}$	$E_{E1}$	$\sigma_{E1}$	$T_f$	$\Gamma_{M1}$	$E_{M1}$	$\sigma_{M1}$	$\Gamma_{SR}$	$E_{SR}$	$\sigma_{SR}$	$C$	$\eta$
	(MeV)	(MeV)	(mb)	(MeV)	(MeV)	(MeV)	(mb)	(MeV)	(MeV)	(mb)	( $10^{-8}$ MeV $^{-3}$ )	(MeV $^{-1}$ )
Lower limit	3.5	16.8	233.0	0.30	2.7	9.5	0.24	2.2	2.8	0.10	4.0	2.5
Upper limit	6.6	17.8	233.0	0.30	2.7	9.5	2.00	2.2	2.8	0.18	5.0	2.5

used the default parameters as implemented in TALYS-1.6. We have found that the ratio between the cross sections using the global potential and the JLM potential reaches a maximum deviation of  $\approx 34\%$  and  $\approx 48\%$  for the proton and neutron potentials, respectively, for the energy ranges  $2.5 \cdot 10^{-6} \leq E_n \leq 5$  MeV and  $0.75 \leq E_p \leq 5$  MeV. On average, the JLM potential gives a lower capture cross section than the global potential for the neutron capture, and opposite for proton capture.

The combined model uncertainties in the cross sections, including the optical-model uncertainties, reach a factor of  $\approx 33$  and  $\approx 36$  at maximum for the  $(n,\gamma)^{89}\text{Y}$  and  $(p,\gamma)^{89}\text{Y}$  cross sections. These can be considered as the intrinsic uncertainties for the models implemented in TALYS (note again that no information is available regarding the level spacing  $D_0$  and the average radiative width  $\langle\Gamma_\gamma\rangle$ ). The results are shown as thick, black lines in Figs. 9 and 10.

## 2. TALYS default predictions.

If no keywords related to level density,  $\gamma$ SF, or proton or neutron potential are specified in the TALYS input file, default values will automatically be invoked. For the  $(n,\gamma)^{89}\text{Y}$  reaction, these are the neutron optical potential [55] with local parameters, the GLo model with variable temperature [34], and the combined constant-temperature plus back-shifted Fermi gas model [59] for the level density. For the  $(p,\gamma)^{89}\text{Y}$  reaction these default values are the same, except for the proton potential, for which there are no local parameters and the global pa-

rameterization of Ref. [55] is used. The results are displayed as black crosses in Figs. 9 and 10.

It is interesting to note that, by default, there is an automatic re-scaling of the  $\gamma$ SF in TALYS to match the estimated  $\langle\Gamma_\gamma\rangle = 170$  meV from the spline-fit interpolation table. However, this procedure does not guarantee that the resulting  $(n,\gamma)$  cross section will be the same for different model combinations of the  $\gamma$ SF and level density. The default-estimate cross section (crosses in Fig. 9) with a scaling factor  $gnorm = 1.44$  is very different from the lower-limit cross section with  $gnorm = 0.28$  (lower, thick black lines in Fig. 9). This demonstrates that there is a delicate interplay with the adopted level density (with its spin distribution),  $\gamma$ SF, and particle optical potential in the calculation of radiative cross sections.

## 3. Results from this work implemented in TALYS.

Finally, we have used our results to constrain the input level density and  $\gamma$ SF for the  $^{88}\text{Y}(n,\gamma)^{89}\text{Y}$  and  $^{88}\text{Sr}(p,\gamma)^{89}\text{Y}$  cross sections and reaction rates. We have used the constant-temperature model for the level density with parameters given in Sec. II C above  $E_x = 2.88$  MeV, with a spin distribution and parameters according to the lower and upper normalizations as described in Sec. II C. This model reproduces our level-density data very well. Below that excitation energy, we use the known, discrete levels. For the  $\gamma$ SF data, we have tuned the  $\gamma$ SF models to reproduce our lower and upper data points. Specifically, we have used a low-lying  $M1$  strength that cor-

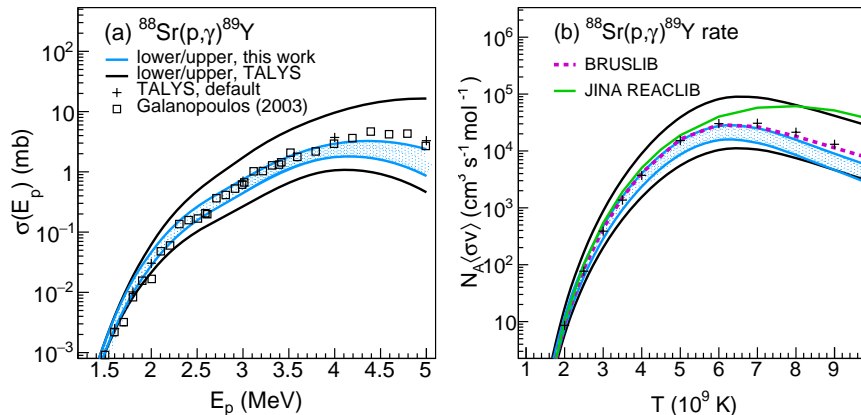


FIG. 10: (Color online) Calculated  $^{88}\text{Sr}(p,\gamma)^{89}\text{Y}$  cross sections shown as a blue-shaded band (a) compared to data from Ref. [63], and the corresponding astrophysical reaction rates (b) compared to the BRUSLIB (dashed magenta line, Ref. [50]) and the JINA REACLIB (green solid line, Ref. [62]). The minimum and maximum predictions from the models implemented in TALYS are also shown (thick, black lines), as well as the result using default input parameters (black crosses).

responds to the shell-model results parameterized as an exponential function  $f_{\text{upbend}} = C \exp -\eta E_\gamma$ , an  $M1$  spin-flip resonance, and a GLo  $E1$  component so as to match our upper and lower limits. In addition, our  $\gamma\text{SF}$  data points overshoot the  $M1 + E1$  models in the energy range of  $E_\gamma \approx 2.0 - 3.5$  MeV, as seen in Figs. 7 and 8. Therefore, we have added a small resonance (SR) of  $M1$  type to get a reasonable agreement with the measured strength. The applied parameters are given in Tab. III. The input  $\gamma\text{SF}$  for  $^{89}\text{Y}$  is shown in Fig. 9(a).

The resulting  $^{88}\text{Y}(n,\gamma)^{89}\text{Y}$  and  $^{88}\text{Sr}(p,\gamma)^{89}\text{Y}$  cross sections are displayed in Figs. 9(b), 10(a) respectively, and shown as blue-shaded bands. We note that our estimated  $(n,\gamma)$  cross section is in the lower region of the uncertainty band provided by TALYS. Also, our error band does not match well with the default TALYS prediction, as our results indicate a significantly lower cross section.

For the  $^{88}\text{Sr}(p,\gamma)^{89}\text{Y}$  cross section, direct measurements exist [63]. Overall, we find a very good agreement between our calculations and the  $^{88}\text{Sr}(p,\gamma)^{89}\text{Y}$  data from Ref. [63], although the data indicate a slightly higher cross section for incoming proton energies  $E_p > 4.3$  MeV. The overall good agreement, however, gives confidence in our approach to estimate radiative capture cross sections, as also demonstrated in Refs. [60, 61].

We have also estimated the astrophysical reaction rates, which are shown in Figs. 9(c), 10(b). We have compared to the BRUSLIB [50] and the JINA REACLIB [62] databases. We find that the BRUSLIB rates are rather similar to our estimated upper limits, especially for the  $(p,\gamma)$  reaction. In contrast, the JINA REACLIB rates are significantly higher both for the proton-capture and neutron-capture cases, especially for higher stellar temperatures.

The low-energy upbend has been shown to increase neutron-capture rates of very neutron-rich nuclei, if it is found to be present in such exotic isotopes [46]. For  $^{89}\text{Y}$ , however,

the impact of the upbend on the cross sections is very limited; for example, for the  $(p,\gamma)$  reaction, the relative change in cross section is at maximum 1%, and for the  $^{88}\text{Y}(n,\gamma)$  reaction maximum 2%. However, provided that the upbend persists for very neutron-rich Y nuclei, it may influence the  $(n,\gamma)$  rates of relevance for the  $r$ -process.

## V. SUMMARY AND OUTLOOK

In this work, we have determined the nuclear level density and  $\gamma\text{SF}$  of  $^{89}\text{Y}$ . The data are available at the following web site: <http://ocl.uio.no/compilation>. We find that this nucleus exhibits a low-energy enhancement in the  $\gamma\text{SF}$ , in accordance with previous findings in this mass region. Moreover, shell model calculations describe the main part of the low-energy enhancement by  $M1$  transitions, similar to previous shell-model results for Mo, Fe, and Zr isotopes. However, as (a contribution of)  $E1$  transitions cannot be ruled out based on the available data, an experimental determination of the electromagnetic character of this enhancement is highly desired to firmly establish the mechanism behind this phenomenon.

We have applied our new data as input for nuclear-reaction calculations, estimating radiative capture cross sections and reaction rates for the reactions  $^{88}\text{Sr}(p,\gamma)^{89}\text{Y}$  and  $^{88}\text{Y}(n,\gamma)^{89}\text{Y}$ . For the radiative proton capture case, we find good agreement with our experiment-constrained calculations and direct measurements. Moreover, in comparison with widely used reaction-rate libraries, we note that the BRUSLIB predictions in general agree better with our results.

In the future, it would be very valuable to measure other nuclei in this mass region with the Oslo method, to be able to further constrain reactions such as  $^{87}\text{Y}(n,\gamma)^{88}\text{Y}$  of importance to the  $p$ -process nucleosynthesis. To be able to reduce the errors

associated with our approach, further developments of independent absolute-normalization techniques would be highly desirable, as well as complementary experiments, such as measurements of particle-evaporation spectra and  $\gamma$ -ray two-step cascade spectra to infer level densities and  $\gamma$ SFs, respectively.

### Acknowledgments

The authors wish to thank J.C. Müller, E.A. Olsen, A. Semchenkov and J. Wikne at the Oslo Cyclotron Laboratory for

providing excellent experimental conditions. This work was financed in part by the Research Council of Norway (NFR), project grant no. 205528, and through the ERC-STG-2014 under grant agreement no. 637686. S. G. is FNRS research associate. S. S. acknowledges financial support by the NFR under project grant no. 210007. M. W. acknowledges support by the National Research Foundation of South Africa under grant no. 92789.

- 
- [1] M. Arnould, S. Goriely, and K. Takahashi, *Phys. Rep.* **450**, 97 (2007).
- [2] M. Arnould and S. Goriely, *Phys. Rep.* **384**, 1 (2003).
- [3] C. Iliadis, *"Nuclear Physics of Stars"*, Wiley-VCH Verlag, Weinheim (2007).
- [4] T. Rauscher, N. Dauphas, I. Dillmann, C. Frölich, Zs. Fülöp, and Gy. Gyürky, *Rep. Prog. Phys.* **76**, 066201 (2013).
- [5] C. Sneden, J. J. Cowan, and R. Gallino, *Ann. Rev. Ast. Ap.* **46**, 241 (2008).
- [6] E. M. Burbidge, G. R. Burbidge, W. A. Fowler, and F. Hoyle, *Rev. Mod. Phys.* **29**, 547 (1957).
- [7] O. Just, A. Bauswein, R. Ardevol Pulpillo, S. Goriely, H.-T. Janka, *Month. Not. Roy. Astron. Soc.* **448**, 541 (2015).
- [8] C. Travaglio, F.K. Röpkke, R. Gallino, W. Hillebrandt, *Astrophys. J.* **739**, 93 (2011).
- [9] W. Hauser and H. Feshbach, *Phys. Rev.* **87**, 366 (1952).
- [10] A. Schiller, L. Bergholt, M. Guttormsen, E. Melby, J. Rekstad, and S. Siem, *Nucl. Instrum. Methods Phys. Res. A* **447**, 498 (2000).
- [11] M. Guttormsen *et al.*, *Phys. Rev. C* **90**, 044309 (2014).
- [12] M. Guttormsen *et al.*, *Phys. Rev. C* **71**, 044307 (2005).
- [13] M. Wiedeking *et al.*, *Phys. Rev. Lett.* **108**, 162503 (2012).
- [14] R. Schwengner, S. Frauendorf, and A. C. Larsen, *Phys. Rev. Lett.* **111**, 232504 (2013).
- [15] R. D. Hoffman, K. Kelley, F. S. Dietrich, R. Bauer, and M. G. Mustafa, UCRL-TR-222275, LLNL (2006); <https://e-reports-ext.llnl.gov/pdf/334904.pdf>.
- [16] M. Guttormsen, A. Bürger, T.E. Hansen, and N. Lietaer, *Nucl. Instrum. Methods Phys. Res. A* **648**, 168 (2011).
- [17] M. Guttormsen, A. Atac, G. Løvholden, S. Messelt, T. Ramsøy, J. Rekstad, T.F. Thorsteinsen, T.S. Tveter, and Z. Zelazny, *Phys. Scr.* **T 32**, 54 (1990).
- [18] M. Guttormsen, T. S. Tveter, L. Bergholt, F. Ingebretsen, and J. Rekstad, *Nucl. Instrum. Methods Phys. Res. A* **374**, 371 (1996).
- [19] M. Guttormsen, T. Ramsøy, and J. Rekstad, *Nucl. Instrum. Methods Phys. Res. A* **255**, 518 (1987).
- [20] A.C. Larsen *et al.*, *Phys. Rev. C* **83**, 034315 (2011).
- [21] D. M. Brink, Ph.D. thesis, Oxford University, 1955.
- [22] P. Axel, *Phys. Rev.* **126**, 671 (1962).
- [23] M. Guttormsen, A. C. Larsen, A. Görgen, T. Renstrøm, S. Siem, T. G. Tornyi, and G. M. Tveten, *Phys. Rev. Lett.* **116**, 012502 (2016).
- [24] A. Bohr and B. Mottelson, *Nuclear Structure*, Benjamin, New York, 1969, Vol. I.
- [25] Data from the NNDC On-Line Data Service database as of March 2015; available at <http://www.nndc.bnl.gov/nudat2/>.
- [26] R. Capote *et al.*, *Nucl. Data Sheets* **110**, 3107 (2009); *Reference Input Parameter Library (RIPL-3)*, available at <http://www-nds.iaea.org/RIPL-3/>.
- [27] T. von Egidy and D. Bucurescu, *Phys. Rev. C* **80**, 054310 (2009).
- [28] L. G. Moretto, A. C. Larsen, F. Giacoppo, M. Guttormsen, S. Siem, and A. V. Voinov, arXiv:1406.2642 [nucl-th], submitted to *Phys. Lett. B* (2015).
- [29] T. von Egidy and D. Bucurescu, *Phys. Rev. C* **72**, 044311 (2005); *Phys. Rev. C* **73**, 049901(E) (2006).
- [30] T. Ericson, *Nucl. Phys.* **11**, 481 (1959).
- [31] T. Ericson, *Adv. Phys.* **9**, 425 (1960).
- [32] S. Goriely, S. Hilaire, and A. J. Koning, *Phys. Rev. C* **78**, 064307 (2008).
- [33] A. Voinov, M. Guttormsen, E. Melby, J. Rekstad, A. Schiller, and S. Siem, *Phys. Rev. C* **63**, 044313 (2001).
- [34] J. Kopecky and M. Uhl, *Phys. Rev. C* **41**, 1941 (1990).
- [35] A. C. Larsen *et al.*, *Phys. Rev. Lett.* **111**, 242504 (2013).
- [36] B. L. Berman, J. T. Caldwell, R. R. Harvey, M. A. Kelly, R. L. Bramblett, and S. C. Fultz, *Phys. Rev.* **162**, 1098 (1967).
- [37] A. Lepretre, H. Beil, R. Bergere, P. Carlos, A. Veyssiere, and M. Sugawara, *Nucl. Phys. A* **175**, 609 (1971).
- [38] V. V. Varlamov, N. N. Peskov, D. S. Rudenko, and M. E. Stepanov, *Vop. At. Nauki i Tekhn., Ser. Yadernye Konstanty* **2003**, 48 (2003).
- [39] S. S. Dietrich and B. L. Berman, *At. Data Nucl. Data Tables* **38**, 199 (1988).
- [40] N. Benouaret, R. Schwengner, G. Rusev, F. Dönau, R. Beyer, M. Erhard, E. Grosse, A. R. Junghans, K. Kosev, C. Nair, K. D. Schilling, A. Wagner, and N. Bendjaballah, *Phys. Rev. C* **79**, 014303 (2009).
- [41] A. Voinov *et al.*, *Phys. Rev. Lett.* **93**, 142504 (2004).
- [42] F. Bečvář, *Nucl. Instrum. Methods Phys. Res. A* **417**, 434 (1998).
- [43] A. Simon *et al.*, accepted for publication in *Phys. Rev. C* (2016); arXiv:1602.05824.
- [44] E. Litvinova and N. Belov, *Phys. Rev. C* **88**, 031302(R) (2013).
- [45] B. Alex Brown and A. C. Larsen, *Phys. Rev. Lett.* **113**, 252502 (2014).
- [46] A. C. Larsen and S. Goriely, *Phys. Rev. C* **82**, 014318 (2010).
- [47] D. Zwarts, *Comput. Phys. Commun.* **38**, 365 (1985).
- [48] S. Goriely, M. Samyn, M. Bender and J. M. Pearson, *Phys. Rev. C* **68** 054325 (2003).
- [49] S. Goriely, E. Khan, and M. Samyn, *Nucl. Phys.* **A739**, 331

- (2004).
- [50] M. Arnould, S. Goriely, Nucl. Phys. **A777**, 157 (2006). *The Brussels Nuclear Library for Astrophysics Applications – BRUSLIB*, maintained by Institut d’Astronomie et d’Astrophysique, Université Libre de Bruxelles; available at <http://www.astro.ulb.ac.be/bruslib/>.
- [51] C. Iwamoto *et al.*, Phys. Rev. Lett. **108**, 262501 (2012).
- [52] G. Rusev *et al.*, Phys. Rev. Lett. **110**, 022503 (2013).
- [53] A. J. Koning, S. Hilaire and M. C. Duijvestijn, "TALYS-1.6", *Proceedings of the International Conference on Nuclear Data for Science and Technology*, April 22-27, 2007, Nice, France, editors O. Bersillon, F. Gunsing, E. Bauge, R. Jacqmin, and S. Leray, EDP Sciences, 2008, p. 211-214.
- [54] A. J. Koning and D. Rochman, Nuclear Data Sheets **113**, 2841 (2012).
- [55] A. J. Koning and J.-P. Delaroche, Nucl. Phys. **A713**, 231 (2003).
- [56] E. Bauge *et al.*, Phys. Rev. C **63**, 024607 (2001).
- [57] S. Hilaire, M. Girod, S. Goriely, and A. J. Koning, Phys. Rev. C **86**, 064317 (2012).
- [58] S. Goriely and E. Khan, Nucl. Phys. A **706**, 217 (2002).
- [59] A. Gilbert and A. G. W. Cameron, Can. J. Phys. **43**, 1446 (1965).
- [60] H. K. Toft, A. C. Larsen, A. Bürger, M. Guttormsen, A. Görge, H. T. Nyhus, T. Renstrøm, S. Siem, G. M. Tveten, and A. Voinov, Phys. Rev. C **83**, 044320 (2011).
- [61] T. G. Tornyi *et al.*, Phys. Rev. C **89**, 044323 (2014).
- [62] R. H. Cyburt *et al.*, Astrophys. J. Suppl. Ser. **189**, 240 (2010); available at <https://groups.nsc1.msu.edu/jina/reaclib/db/>.
- [63] S. Galanopoulos *et al.*, Phys. Rev. C **67**, 015801 (2003).